Rational design of Ru species on N-doped graphene promoting water dissociation for boosting hydrogen evolution reaction

Zhida Chen[1], Wenda Chen[1], Lirong Zheng[4], Tao Huang[1], Jing Hu[1], Yaqi Lei[1], Qi Yuan[1], Xiangzhong Ren[1], Yongliang Li[1], Lei Zhang[1], Shaoluan Huang[3], Shenghua Ye[1,3*], Qianling Zhang[1*], Xiaoping Ouyang[5*], Xueliang Sun[2*] & Jianhong Liu[1,3*]

[1]Graphene Composite Research Center, Shenzhen University, College of Chemistry and Environmental Engineering, Shenzhen University, Shenzhen 518060, China;
[2]Department of Mechanical and Materials Engineering, University of Western Ontario, London, Ontario N6A 5B9, Canada;
[3]Shenzhen Eigen-Equation Graphene Technology Co. Ltd., Shenzhen 518000, China;
[4]Institute of High Energy Physics Chinese Academy of Sciences, Beijing 100049, China;
[5]School of Materials Science and Engineering, Xiangtan University, Xiangtan 411105, China

In this study, the morphological distribution of Ru on nitrogen-doped graphene (NG) could be rationally regulated *via* modulating the combination mode between Ru precursor and the zeolite imidazolate framework-8 (ZIF-8). The cation exchange and host-guest strategies respectively resulted in two different combination modes between Ru precursor and ZIF-8 anchored on graphene. Following pyrolysis of the above precursors, Ru single-atom sites (SASs) with and without Ru nanoparticles (NPs) were formed selectively on NG (denoted as Ru SASs+NPs/NG and Ru SASs/NG, respectively). Ru SASs+NPs/NG exhibited excellent hydrogen evolution reaction (HER) performance in alkaline solutions (η_{10}=12 mV, 12.57 A mg$^{-1}_{Ru}$ at 100 mV), which is much better than Ru SASs/NG. The experimental and theoretical study revealed that Ru SASs could adsorb hydrogen with optimal adsorption strength, while Ru NPs could lower the barrier of water molecule dissociation, and thus Ru SASs and Ru NPs could synergistically promote the catalytic performance of HER in alkaline solutions.

Ru, single atomic sites, nanoparticles, water dissociation, synergistic effect

1   Introduction

As one of the renewable energy resources, exhibiting high energy density and non-polluting characteristics, hydrogen is regarded as an essential candidate to address the depletion of fossil fuel resources and remediate the various environmental issues [1–6]. Here, water splitting is regarded as a potential avenue to generate high-purity hydrogen on a large scale [7]. The water splitting is consisted of the hydrogen evolution reaction (HER) and the oxygen evolution reaction (OER). Given that few OER catalysts composed of transition metal can remain stable in highly corrosive acidic environments under oxidizing potentials [8–11], water splitting in alkaline solutions remains the preference for industrial applications. Thus, exploring alkaline-based HER electrocatalysts is of great interest [12,13].

Alkaline-based HER is energy-intensive, and even when using the most active catalysts (*e.g.*, platinum [Pt]), it is two or three orders of magnitude less efficient than that under

---

acidic conditions [14,15]. This issue is because of the fact that the HER in alkaline solutions involves water dissociation for the release of protons, and overcoming the barrier of water dissociation remains a challenging pursuit [16–19]. Moreover, although Pt, ruthenium (Ru), and iridium (Ir) have been recognized as efficient HER catalysts because of their moderate M–H bonding, their practical availabilities are hindered by their high-cost and comparative scarcity [20]. Meanwhile, how to reduce the precious metal loading without sacrificing the catalytic activity remains the main challenge.

Consequently, single-atom catalysts (SACs) received great attention because of their ultra-high atom utilization and ultra-low metal loading [21–23]. Ultra-thin two-dimensional (2D) nanomaterials such as graphene and MXenes are ideal substrates for loading single atomic sites due to their large specific surface area, excellent electronic conductivity, and outstanding resistance to corrosion [24]. Certain transition-metal-based SACs have also been found to present outstanding HER activity, which originates from the co-ordinative unsaturated metallic sites [25–30]. In brief, these SACs are composed mainly of an MN_4 (M represents the metal element) structure with appropriate hydrogen adsorption/desorption strength (ΔG_{H*}). However, for the most part, these SACs are applied commonly in acidic solutions, and few studies have considered their HER activity in alkaline solutions. The reasons are summarized as follow: Generally, the HER in acidic solutions involves the direct adsorption and reduction of protons at MN_4 sites which usually exhibits high catalytic activity due to the feature of unsaturated co-ordinative structure. However, the situation in alkaline solutions is quite complicated. The foremost is accelerating water adsorption and dissociation at appropriate sites to release protons [31–33]. Subsequently, the generated two adsorbed species of H* and OH* require at least two adsorption sites, and H* should be adsorbed on catalytic sites to be converted to hydrogen. SACs featured by solely isolated atomic sites do not meet this crucial requirement. Therefore, rational design of active sites for water dissociation on the SACs is the key to solving the above dilemma.

Herein, we utilized metal organic framework-assisted pyrolysis to regulate the morphological distribution of Ru anchored on nitrogen-doped graphene (NG). Using the cation exchange and the host-guest strategies to render Ru³⁺ anchored onto the zeolite imidazolate framework-8 (ZIF-8), we found that the morphological distribution of Ru on graphene is related to the combination mode between the Ru³⁺ and the ZIF-8. Following pyrolysis of the precursors, Ru single-atom sites (SASs) with and without Ru nanoparticles (NPs) were formed exclusively on NG (denoted as Ru SASs +NPs/NG and Ru SASs/NG, respectively). Overall, as prepared Ru SASs+NPs/NG with the mole ratio of SASs to NPs approximate to 1:1 exhibited extremely high catalytic ac-

tivity in 1 M KOH solution, which is superior to Ru SASs/NG, Ru NPs/NG, commercial Pt/C (20 wt%), and Ru/C (5 wt%). Meanwhile, the density functional theory (DFT) study demonstrated that Ru NPs not only worked as active sites for promoting water dissociation to generate H* adsorbed on Ru SASs but also optimized the adsorption/desorption strength of H* on Ru SASs, thus greatly accelerating the HER process.

2 Experimental

2.1 Materials

All the chemical reagents were purchased from Aladdin. Single-layer graphene was produced from Shenzhen Eigen-Equation Graphene Technology Co., Ltd. (Shenzhen, China) and synthesized from liquid acrylonitrile homopolymer.

2.2 Catalyst preparation

For the synthesis of Ru SASs+NPs/NG, first, 40 mg of graphene was dispersed in 20 mL of methanol, with the addition of 224 mg of $Zn(NO_3)_2 \cdot 6H_2O$ during ultrasonic treatment for 30 min to achieve a uniformed dispersion. Another sample of 20 mL methanol containing 246 mg of dimethylimidazole was slowly injected into the as-obtained dispersion, which was then stirred magnetically for 12 h to achieve a ZIF-8 anchored on the graphene. The resulting product ZIF-8/G was collected by centrifugation after being washed with methanol several times and was then re-dispersed in 30 mL methanol. Following this, 120 μL of $RuCl_3 \cdot 3H_2O$ (20 g/L) was added to the ZIF-8/G dispersion. After being stirred magnetically for 3 h, the Ru-ZIF-8/G was harvested by centrifugation after being washed with methanol (the supernatant liquor was almost colourless, indicating that all of Ru³⁺ ions have been anchored on ZIF-8). The Ru-ZIF-8/G was then placed in a tube furnace and heated to 400 °C at a heating rate of 5 °C/min for 1 h, before being heated to 900 °C for 2 h under inert gas. The Ru SASs+NPs/NG was thus synthesized. The series Ru percentages of Ru SASs+NPs/NG samples were synthesized by adding different volumes of $RuCl_3$ (Table S1, Supporting Information online).

For the synthesis of Ru SASs/NG, first, 40 mg of graphene was dispersed in 20 mL of methanol, with the addition of 224 mg of $Zn(NO_3)_2 \cdot 6H_2O$ and 100 mg of Ru acetylacetonates ($Ru[acac]_3$). The above solution was transferred for ultrasonic treatment for 30 min to achieve a homogeneous dispersion. Another 20 mL solution of methanol containing 246 mg of dimethylimidazole was dispensed into the as-obtained dispersion and was stirred magnetically for 12 h, whereupon $Ru(acac)_3$ was encapsulated into the ZIF-8 anchored on graphene (Ru@ZIF-8/G). The Ru@ZIF-8/G

was washed with methanol then harvested by centrifugation for several times (the supernatant liquor was red, indicating that Ru(acac)$_3$ was excess, and only small amount of Ru(acac)$_3$ was encapsulated into the ZIF-8). Ru SASs/NG was synthesized following pyrolysis, using the same process as that used for the Ru SASs+NPs/NG.

In terms of the synthesis of NG, the same process was used as that of Ru SASs+NPs/NG, with the exception of the addition of Ru precursor. For synthesis of Ru NPs/NG, NG was dispersed into H$_2$O under supersonic to form a uniform dispersion, and then certain of RuCl$_3$ was mixed into the NG dispersion. Subsequently, exceeded NaBH$_4$ was added into above solution during magnetic stirring to guarantee that RuCl$_3$ had been reduced thoroughly. After filtration and drying in vacuum, Ru NPs/NG was prepared.

2.3   Catalyst characterization

Field emission scanning electron microscopy (FE-SEM, JSM-7800F), transmission electron microscopy (TEM, JEOL-F200) and scanning transmission electron microscope (FEI Titan Cubed Themis G2 300) were used for morphologies observation. X-ray photoelectron spectroscopy (XPS, ESCALAB 250) with C 1s calibrated to 284.4 eV was used for chemical state analyses. The metal loading of samples was detected by inductively coupled plasma-mass spectrometry (ICP-MS, TJA IRIS (HR)). Raman spectroscopy (Renishaw, inVia) was used for characterization of graphene. Meanwhile, the X-ray near edge absorption structure (XANES) measurements of the Ru K-edges was performed using the hard X-ray microanalysis beamline by a solid-state detector with fluorescence yield, and the Ru powder spectra for comparison and for monochromatic energy calibration.

2.4   Electrochemical measurements

The catalytic performance was evaluated using a CHI660E electrochemical analyzer (CH Instruments, Inc., Shanghai) in the reversible hydrogen electrode, in which glass carbon (GC) electrode, graphite rod and saturated calomel electrode (SCE) were used as working electrode, counter electrode and reference electrode, respectively. All the potentials were calibrated to the reversible hydrogen electrode ($E_{RHE}= E_{SCE}$+1.068 V). Finally, the linear sweep voltammetry (LSV) measurements were corrected using *iR* compensation. The loading of the catalyst on the GC electrode was 0.707 mg cm^{-2}.

The electrochemically active surface area (ECSA) and active site density could be obtained through an analysis of the copper underpotential deposition (Cu-upd) method, which was validated successfully for the Ru-Pt surfaces. The detailed performance steps and the calculation method are outlined below [34,35].

Step 1: The CV curves of the catalyst were recorded as the background at the potential range of 0.23–0.7 V *vs*. RHE in 0.25 M H$_2$SO$_4$ at a scan rate of 10 mV s^{-1} for Ru SASs+NPs/NG and Ru SASs/NG.

Step 2: The CV curves in the 0.25 M H$_2$SO$_4$+10 mM CuSO$_4$ solution were recorded at the above potential range and scan rate. The Cu-upd was commenced at ~0.45 V and lasted to ~0.23 V at the cathodic scan. The as-formed Cu-upd adlayer was stripped during the positive scan.

Step 3: The number of active Ru sites could be calculated by integrating the Cu-upd adlayer stripping area, which was determined by subtracting the background measured in 0.25 M H$_2$SO$_4$ solution.

Step 4: For Pt/C and Ru/C, the CV curves were recorded at the potential range of 0.23–0.9 V and −0.07–0.45 V, respectively.

Step 5: Assuming a value of 420 μC cm^{-2} for a saturated Cu-upd monolayer formation on active metal sites, the ECSA could be calibrated using the following equation:

$$ECSA = \frac{Q_{Cu}}{M_{Ru\ or\ Pt} \times 420\ \mu C\ cm^{-2}} \tag{1}$$

where M is the mass loading of the metal on a certain geometric area of the working electrode.

Step 6: The active sites was quantified by the coulombic integration of the Cu-upd adlayer stripping.

The turnover frequency (TOF) value could finally be calculated using the following formula:

$$TOF = JA/2Fm \tag{2}$$

where the TOF is based on the number of redox-active sites, J is the current density at a certain overpotential, A is the area of the electrode, 2 indicates the moles of electrons consumed for the evolution of one mole of H$_2$ from H$_2$O, F is the Faraday constant, and m is the number of moles of the active sites.

2.5   DFT calculations

The principle calculations in the DFT framework were conducted based on the Cambridge Sequential Total Energy Package (CASTEP) [36]. The interaction of electrons was elucidated using exchange-correlation functional under the generalized gradient approximation (GGA) [37]. The convergence was investigated with a *k*-point of 5×5×1 and an energy cutoff located at 750 eV (force tolerance: 0.01 eV Å^{-1}, energy tolerance: 5.0×10^{-7} eV per atom, and maximum displacement: 5.0×10^{-4} Å). All of atoms in the storage models were not constrained with enthalpy. To avoid interactions of neighboring images, vacuum space (*z* direction) was set to 15 Å. All calculations underwent the Grimme method for DFT-D2 correction [38].

The adsorption energy of H was expressed as follows:

$$\Delta E = E*_H - (E* + E_H) \tag{3}$$

where the adsorption of the H atom on the substrates, the bare substrates and half the energy of H_2 were presented as *H, * and E_H, respectively.

The free energy change ΔG of the reaction was calculated as the difference between the free energies of the initial and final states, as shown below:

$$\Delta G = \Delta E + \Delta ZPE - T\Delta S \qquad (4)$$

where E presents the energy calculated by DFT, ZPE denotes the zero-point energy, and the entropy is presented as S. $\Delta ZPE - T\Delta S = 0.24$ eV [21], $\Delta G = \Delta E + 0.24$ eV.

2.6 *Ab initio* molecular dynamics (AIMD) simulation

The Vienna *ab initio* simulation package was conducted in all the first-principle spin-polarized models [39,40]. GGA [41] with Perdew-Burke-Ernzerhof functional [42], plane-wave basis set (cutoff energy: 500 eV) and projector augmented wave method were conducted to elucidate ion-electron interactions. Meanwhile, the convergence threshold was set as 10^{-5} eV and 5×10^{-3} eV Å^{-1}, respectively, during the structure relaxation. DFT+D3 method was used for the weak interaction simulation [43]. Here, supercells were composed of $6 \times 7 \times 1$ graphene unit cells, whereas the Brillouin zones were sampled using Monkhorst-Pack k-point mesh with a $3 \times 3 \times 1$ k-point grid. A vacuum space exceeding 15 Å was used to avoid the interaction between two periodic units. For the initial AIMD structure, a Ru_4 cluster was placed above the hexagonal hole of the graphene.

3 Results and discussion

3.1 Morphology and structure

As depicted in Scheme 1, Ru SASs+NPs/NG and Ru SASs/ NG were synthesized using the cation exchange strategy and the host-guest strategy, respectively. For the cation exchange strategy, ZIF-8 was fabricated on graphene before the Zn^{2+} in the nodes of ZIF-8 was exchanged with Ru^{3+}, as the stronger coordinative ability of Ru^{3+} ions ensured that the resulting Ru was coordinated within the skeleton of the ZIF-8 (denoted as Ru-ZIF-8/G), and the amount of Ru anchored to ZIF-8 increased with the increase of Ru^{3+} feeding. Here 120 μL of $RuCl_3$ solution was added, and the corresponding sample was selected as a representation for further characterization. Meanwhile, for the host-guest strategy, based on the prerequisite that ZIF-8 with a cavity diameter of 11.6 Å serves as the host and the $Ru(acac)_3$ molecule with a diameter of ~10.4 Å acts as the guest, $Ru(acac)_3$ could be encapsulated into the cavities of the ZIF-8 to form Ru@ZIF-8/ G during the growing process of the ZIF-8 [44], and ZIF-8 could be saturated by a certain amount of $Ru(acac)_3$ (different combination modes between Ru precursor and ZIF-8

are illustrated by the Fourier transform infrared (FTIR) spectra in Figure S2 in the Supporting Information online). Following this, the Ru-ZIF-8/G and Ru@ZIF-8/G were pyrolyzed at 900 °C, with the resulting ZIF-8 completely integrated into the graphene matrix (Figures S3 and S4), eventually forming Ru SASs with and without Ru NPs anchored on the NG (denoted as Ru SASs+NPs/NG and Ru SASs/NG, respectively). As a result, ZIF-8 was integrated into the graphene matrix during pyrolysis even in the absence of Ru species (Figure S5), which is in agreement with the previous studies [45,46], whereas the derived carbon remained when annealing Ru-ZIF-8 and Ru@ZIF-8 without graphene (Figures S6 and S7).

The morphology and structure were characterized by SEM and TEM. The SEM and TEM images of the Ru SASs+NPs/ NG indicated that Ru NPs with a diameter of about 2 nm were uniformly anchored on NG without any residual polyhedron derived from the ZIF-8 (Figure 1a, b), suggesting that the ZIF-8 was completely integrated into the graphene matrix to form NG. The lattice spaces of the Ru NPs were estimated to be ~0.21 nm and could be assigned to the (002) facet of the hexagonal Ru (PDF-#06-0663) (Figure 1c). Meanwhile, the high-angle annular dark-field scanning transmission electron microscopy (HAADF-STEM) imaging and the corresponding energy-dispersive X-ray spectroscopy (EDS) mapping demonstrated that C, N, and Ru elements were distributed within the graphene matrix (Figure 1d). The aberration-corrected HAADF-STEM (AC HAADF-STEM) imaging with low magnification confirmed that the Ru NPs were dispersed uniformly (Figure 1e). Furthermore, the high-magnification images revealed that dense Ru SASs surrounded the Ru NPs (Figure 1f), indicating the formation of Ru SASs combined with Ru NPs. In terms of the Ru SASs/ NG, the TEM and HR-TEM images suggested the presence of a graphene matrix with an absence of NPs (Figure 1g, h), whereas the AC HAADF-STEM images revealed discrete bright dots on the graphene matrix (Figure 1i), and the EDS mapping indicated that C and N elements were uniformly distributed but Ru was barely detected (Figure S8), suggesting that Ru SASs were successfully synthesized.

The mass percentage of Ru was measured using ICP-MS. For the host-guest strategy, $Ru(acac)_3$ was excess to guarantee that ZIF-8 has been saturated with $Ru(acac)_3$. The loading of Ru in the Ru SASs/NG was determined to be 0.24 wt%, suggesting that only small amount of $Ru(acac)_3$ could be encapsulated in the cavities of ZIF-8, which is consistent with literature report [43]. For the cation exchange strategy, the amount of Ru anchored on the sample increased with the increase of Ru^{3+} feeding because Ru^{3+} could exchange the Zn^{2+} persistently. By feeding various amounts of $RuCl_3$, a series of Ru SASs+NPs/NG with Ru percentages ranging from 0.07 wt% to 1.91 wt% could be synthesized (listed in Table S1), and the representative sample with a
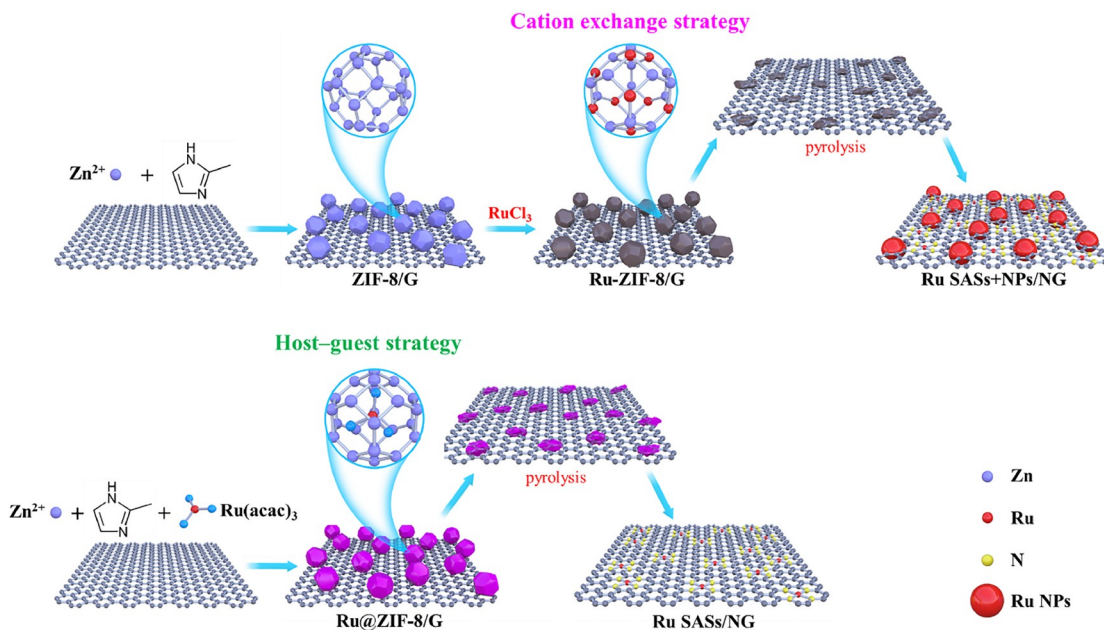
Scheme 1 Synthetic scheme of Ru SASs+NPs/NG and Ru SASs/NG (color online).

120 μL RuCl$_3$ solution was determined to be 1.21 wt%. In the TEM images of the above series (Figures S9–S13), the Ru NPs could be clearly observed, even if the Ru percentage of the Ru SASs+NPs/NG was as low as 0.07 wt% (even lower than that of Ru SASs/NG). This phenomenon implies that the cation exchange pyrolysis strategy is likely to exclusively form an Ru SASs+NPs structure, verifying that the morphological distribution of Ru on NG could be regulated by a different interaction between the Ru precursor and the ZIF-8. Moreover, the pyrolysis temperature affected the morphology of the Ru in the Ru SASs+NPs/NG (Figures S14 and S15).

The X-ray diffraction (XRD) patterns are depicted in Figure 2a. The absence of diffraction for ZIF-8 and Zn species verified that ZIF-8 had been decomposed and Zn had been vapored during pyrolysis. The Ru SASs+NPs/NG and Ru SASs/NG exhibited no clear diffraction for Ru species, but typical broad peaks of graphene at around 26.3° and 44.3°, indicating an absence of large Ru NPs in the Ru SASs/NG and Ru SASs+NPs/NG. X-ray photoelectron spectroscopy (XPS) was also implemented for further examinations of the chemical state. Figure 2b suggested that nitrogen was introduced by decomposition of ZIF-8, and Ru SASs+NPs/NG and Ru SASs/NG exhibited peaks of Ru, N, O, and C elements. The high-resolution N 1s spectra could be fitted into four specific peaks: pyridinic N (398 eV), pyrrolic N/Ru-N$_x$ (399–400 eV), graphitic N (401 eV), and oxidized N (403.9 eV) (Figure 2c) [47,48]. Meanwhile, the high-resolution Ru 3p spectra of the Ru SASs+NPs/NG (Figure 2d) could be fitted into four peaks, 461.9 and 483.8 eV for Ru^0, and 464.9 and 486.4 eV for Ru-N$_x$ [47,48], suggesting the

coexistence of Ru SASs and Ru NPs. However, the Ru signal could not be resolved in the Ru SASs/NG because of the ultra-low loading.

X-ray absorption fine structure (XAFS) studies were performed at the 1W1B station of Beijing Synchrotron Radiation Facility (BSRF) to further illuminate the valence state and coordination structure of Ru. The X-ray absorption near-edge structures (XANES) of Ru K-edge of Ru SASs+NPs/NG and Ru SASs/NG demonstrated that their white line intensities and positions lay between RuO$_2$ and Ru powder (Figure 2e and Figure S16), confirming that the average oxidation states of the Ru in Ru SASs+NPs/NG and Ru SASs/NG were between 0 and +4. Meanwhile, Figure 2f presents the Fourier transformed extended X-ray absorption fine structure (FT-EXAFS). In terms of the Ru SASs/NG, only one dominating peak at the first coordinative shell ascribed to the Ru-N pathway could be identified. The absence of Ru-Ru pathway indicated that all the Ru atoms in Ru SASs/NG in single-atom form were coordinated with the N ligands. With regard to the Ru SASs+NPs/NG, two primary peaks ascribed to the Ru-N pathway at the first coordinative shell and the Ru-Ru pathway at the second coordinative shell could be identified, verifying the coexistence of Ru SASs and Ru NPs in Ru SASs+NPs/NG. The wavelet transformation (WT) of the Ru K-edge (Figure S18) further confirmed the above results. Meanwhile, the fitting result indicated that the coordinative number of the Ru-N in Ru SASs/NG was 4 (Figure S19 and Table S2), suggesting that the Ru SASs was likely to take the form of a typical planar RuN$_4$ motif (Figure S20). Given the coexistence of Ru SASs and Ru NPs, the chemical structure of the Ru SASs+NPs/NG
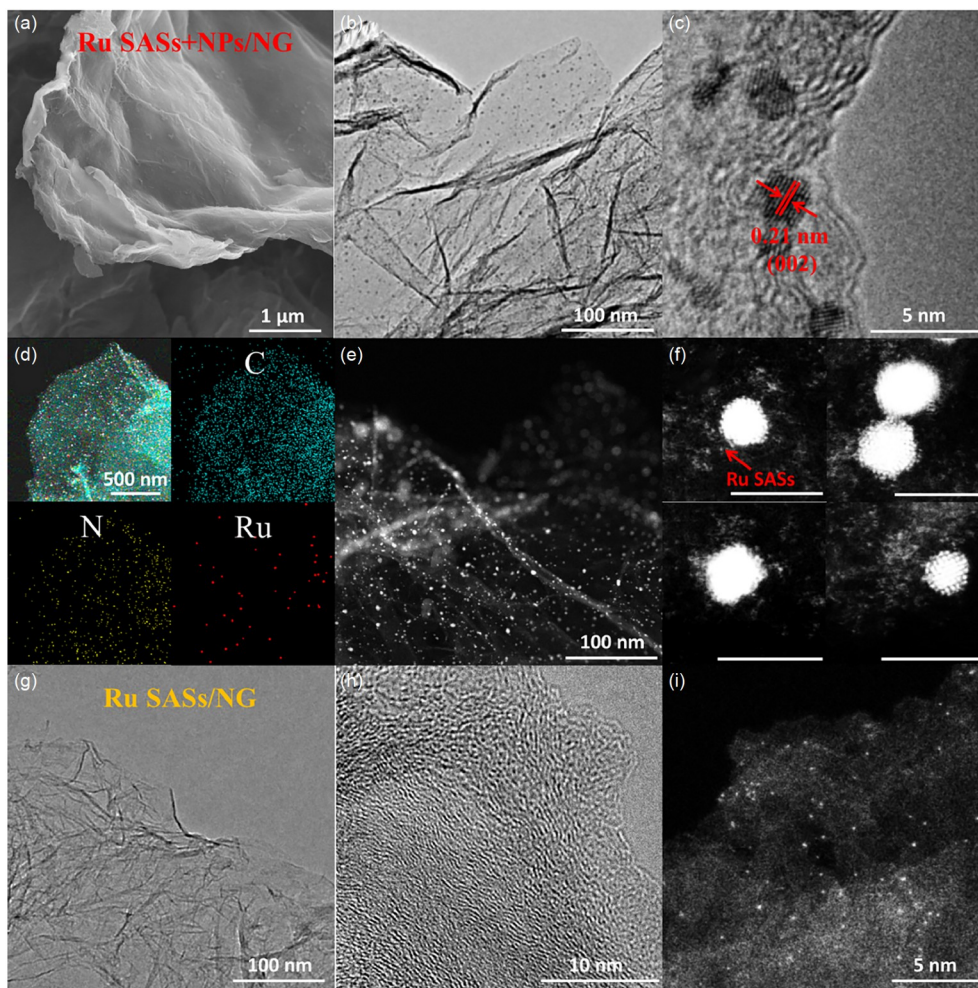
Figure 1 (a) SEM image, (b) low- and (c) high-magnification TEM images of the Ru SASs+NPs/NG; (d) EDS mapping of C, N, and Ru in the Ru SASs +NPs/NG; AC HAADF-STEM images of the Ru SASs+NPs/NG with (e) low- and (f) high-magnification, the bright dots densely dispersing around the Ru NPs represent Ru SASs (the scale bar in (f) is 5 nm); (g) low- and (h) high-magnification TEM images; (i) AC HAADF-STEM image of the Ru SASs/NG (color online).

could be inferred accordingly, as shown in Figure 2g. To further confirm the above structure, linear combination fitting (LCF) analysis was utilized. As shown in Figure 2h, the XANES of Ru SASs+NPs/NG could be perfectly fitted by utilizing the XANES of Ru SASs/NG and Ru powder as parents. This result unquestionably confirmed that Ru SASs +NPs/NG was composed of RuN_4 sites and Ru NPs. In terms of quantification, the molar ratio of the RuN_4 sites and the Ru NPs in Ru SASs+NPs/NG was determined to be 0.52 and 0.48, respectively (close to 1:1), using LCF analysis.

Furthermore, AIMD simulation [49] was used to demonstrate the inevitability of RuN_4 formation in Ru SASs+NPs/NG. As shown in Figure 2i, single Ru atoms tended to diffuse from the metallic Ru to the graphene and become embedded into a neighboring N_4 vacancy at 900 °C. After the formation of RuN_4, the total energy decreased relatively to the initial state of an isolated N_4 vacancy and metallic Ru. Generally, this is the driving force of the spontaneous formation of

RuN_4. The AIMD simulation also suggested that this process requires only hundreds of femtoseconds (10^{-12} s). Overall, the above experimental and simulation results indicated that the formation of single-atom sites of RuN_4 is both spontaneous and inevitable during the pyrolysis of NG and Ru NPs.

For comparision, Ru nanoparticle grown on NG (denoted as Ru NPs/NG) with ~1.21 wt% of Ru was also synthesized by chemical reduction (experimental details are shown in Section 2.3). TEM images in Figure S21a, b suggests that Ru NPs with a diameter of 2–5 nm were dispersed on NG. Ru SASs cannot be observed in AC HAADF-STEM image (Figure S21c), and thus Ru NPs/NG was successfully synthesized. The XRD pattern of Ru NPs/NG (Figure S22) exhibited no clear diffraction for the Ru species, indicating an absence of large Ru NPs. And XPS results (Figure S23) also verified that Ru has been thoroughly reduced. Thus, Ru NPs/NG as a counterpart also has been successfully fabricated.
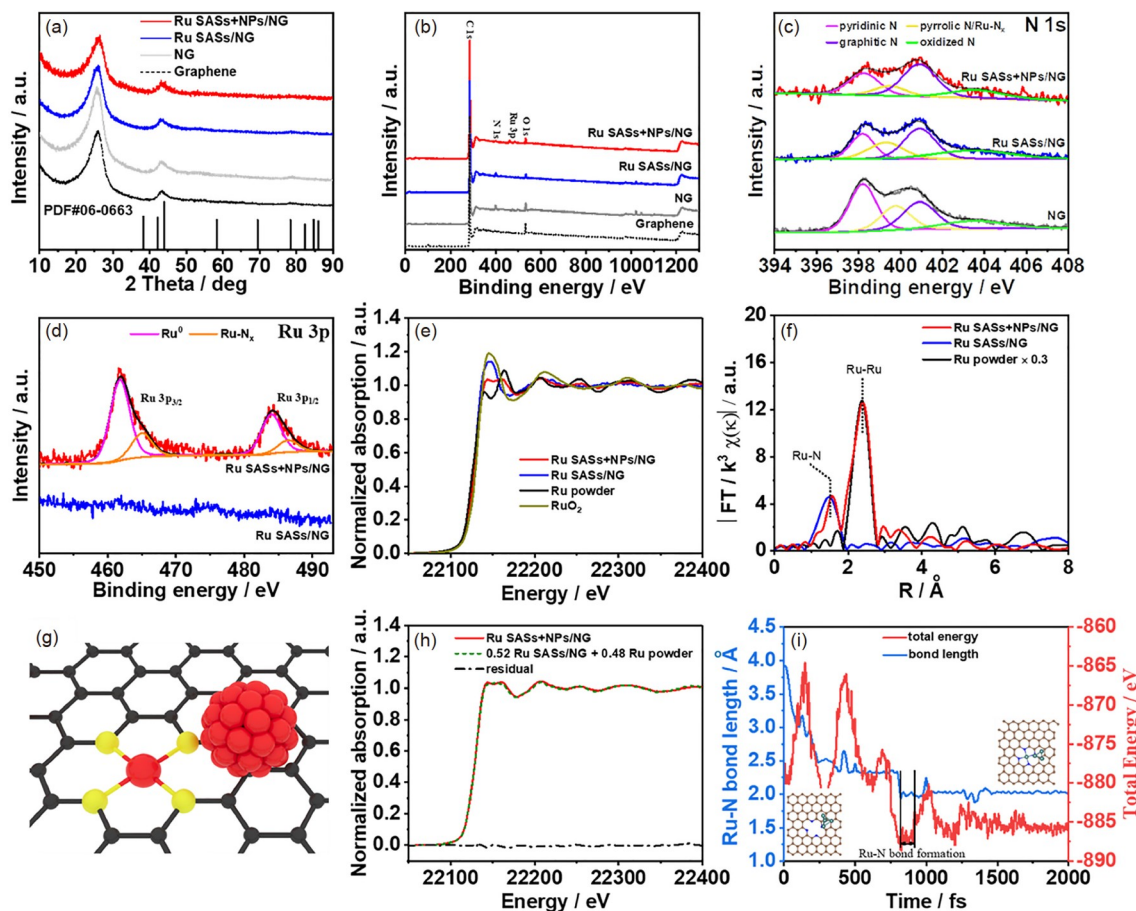
Figure 2   (a) XRD patterns of Ru SASs+NPs/NG, Ru SASs/NG, NG and graphene; XPS of (b) survey, (c) N 1s and (d) Ru 3p of samples; (e) XANES spectra and (f) FT-EXAFS of Ru K-edge for Ru SASs+NPs/NG, Ru SASs/NG, RuO₂ and Ru powder; (g) schematic structure of RuN₄ and Ru NPs in Ru SASs+NPs/NG; (h) LCF of Ru K-edge of Ru SASs+NPs/NG; (i) molecular dynamics simulation showing the formation of a RuN₄ site from Ru NPs at 900 °C (color online).

3.2   Electrochemical performances

The HER activity of different loadings of Ru species and pyrolysis temperature was explored using LSV at a scan rate of 2 mV s⁻¹ in a 1 M KOH solution. Among the Ru SASs +NPs/NG samples with different loadings of Ru, the catalyst with a loading of 1.21 wt% Ru species represented the most optimal catalytic activity (Figure S24). As depicted in Figures S9–S12 and Figure 1, the diameter of Ru and NPs became large when the loading of Ru is higher than 1.21 wt%, indicating that higher loading induced aggregation of Ru and thus reduced the metallic utilization. So Ru SASs+NPs/NG with 1.21 wt% Ru presented optimal loading and metallic utilization to guarantee optimal catalytic activity, which was selected to further study the alkaline HER activity. As shown in Figure 3a, NG was HER inert, and the Ru SASs+NPs/NG required only 12 mV for achieving 10 mA cm⁻², which was obviously lower than that of the Ru SASs/NG (190 mV) and even better than that of commercial 20 wt% Pt/C (24 mV) and 5 wt% Ru/C (35 mV). Furthermore, Tafel slopes were used to characterize the HER kinetics and mechanism of the
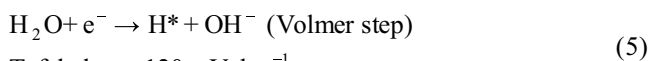
Ru SASs+NPs/NG, Ru SASs/NG, Pt/C and Ru/C. As shown in Figure 3b, the Ru SASs+NPs/NG presented a Tafel slope of 36.6 mV dec⁻¹, which was much lower than that of the Ru SASs/NG (117.1 mV dec⁻¹) and Ru/C (77.5 mV dec⁻¹), but in close proximity to that of the Pt/C (34.28 mV dec⁻¹), demonstrating that Ru SASs+NPs/NG presented the fastest reactive kinetics. The exchange current density of Ru SASs +NPs/NG (4.76 mA cm⁻²) also transcended that of Pt/C (4.10 mA cm⁻²). This catalytic activity of Ru SASs+NPs/NG surpassed that of most state-of-the-art precious-metal-based electrocatalysts (Figure 3c and Table S3).

It is important to further understand the origination of intrinsic catalytic activity. Here, the activity comparison of Ru SASs+NPs/NG and Ru SASs+NPs (Figure S25) suggested that the graphene matrix is crucial for the HER activity because of the excellent electronic conductivity that graphene provides. Here, SCN⁻ was used to block the Ru site (including the metallic sites and SASs) to confirm the activity origination [36]. As shown in Figure S26, a large current density decay was observed toward Ru SASs+NPs/NG and Ru SASs/NG when SCN⁻ was added to the electrolyte,
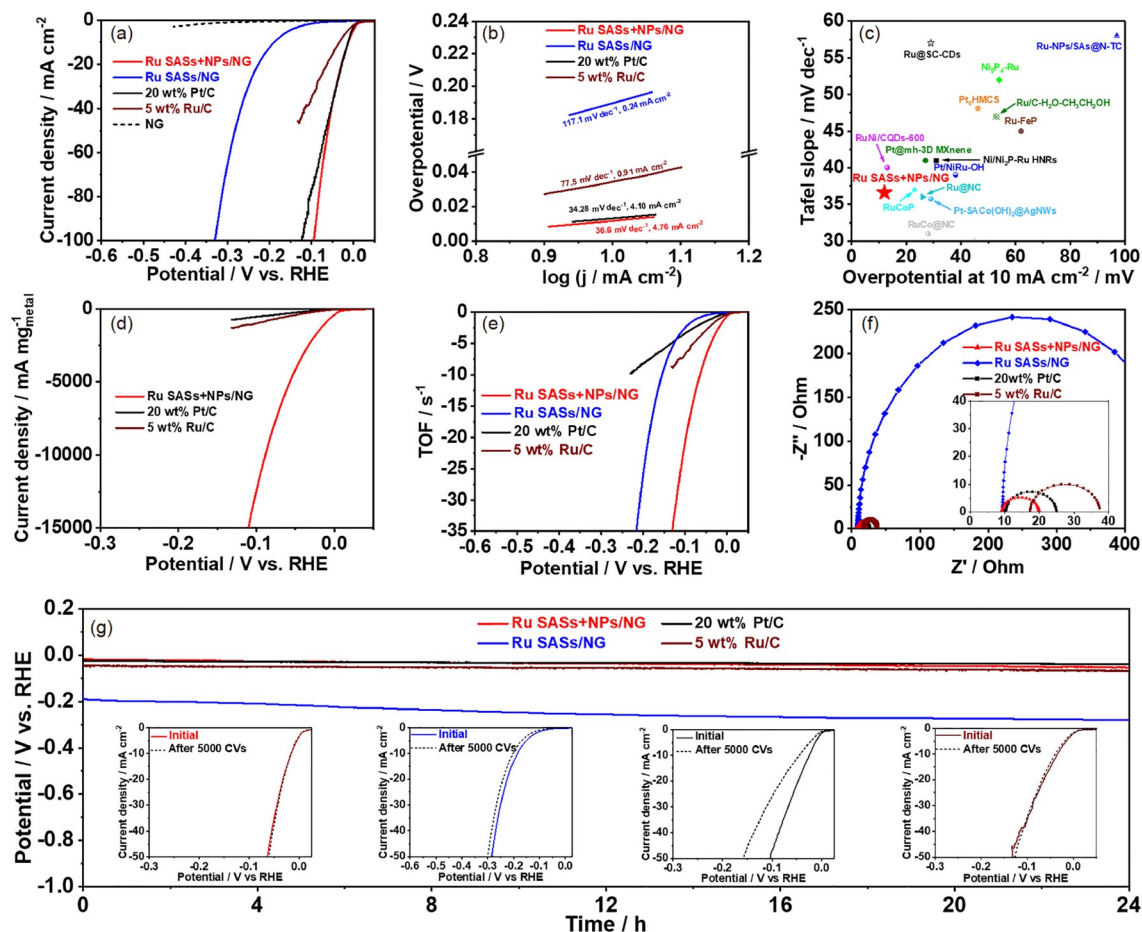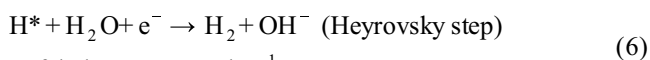
Figure 3 (a) LSV curves of the Ru SASs+NPs/NG, Ru SASs/NG, Pt/C, Ru/C and NG with scan rate at 2 mV s⁻¹ following *iR* correction; (b) Tafel plots of the Ru SASs+NPs/NG, Ru SASs/NG, Pt/C and Ru/C; (c) catalytic activity comparison of Ru SASs+NPs/NG and state-of-the-art precious-metal-based electrocatalysts; (d) LSV curves of the Ru SASs+NPs/NG, Pt/C and Ru/C with scan rate at 2 mV s⁻¹ (normalized to the mass of precious metal); (e) TOF curves and (f) electrochemical impedance spectroscopy (EIS) plots at −0.1 V *vs*. RHE of the Ru SASs+NPs/NG, Ru SASs/NG, Pt/C and Ru/C; (g) *E-t* curves of the Ru SASs+NPs/NG, Ru SASs/NG, Pt/C and Ru/C at a current density of 10 mA cm⁻² (insert graphs: LSV curves of the SASs+NPs/NG, Ru SASs/NG, Pt/C and Ru/C respectively, before and after 5,000 CVs) (color online).

suggesting that the main active sites were likely to be Ru. Therefore, the catalytic processes on Ru and the synergistic effect were further studied. In alkaline solutions, water dissociation and hydrogen adsorption/desorption strength are two crucial factors for the catalytic activity. To further confirm the synergistic effect between Ru SASs and NPs, LSV curves and Tafel plots of Ru SASs+NPs/NG, Ru SASs/NG and Ru NPs/NG were compared. As shown in Figure S27a, Ru NPs/NG exhibited inferior HER activity. The Tafel plots (Figure 3b and Figure S27b) suggested that Ru SASs+NPs/NG obeyed the Volmer-Heyrovsky route with the Heyrovsky step denoted by the rate-determining step (RDS), and the Volmer step by the RDS of Ru SASs/NG and Ru NPs/NG:

$$H_2O + e^- \rightarrow H^* + OH^- \quad \text{(Volmer step)}$$

Tafel slope: 120 mV dec⁻¹

$$(5)$$

$$H^* + H_2O + e^- \rightarrow H_2 + OH^- \quad \text{(Heyrovsky step)}$$

Tafel slope: 39 mV dec⁻¹

$$(6)$$

where * represents adsorbed intermediate species.

Tafel plots demonstrate that Ru SASs/NG and Ru NPs/NG had difficulty in capturing H⁺ from H₂O because of the low dissociation constant of H₂O ($K_w = 1 \times 10^{-14}$). In terms of the Ru SASs+NPs/NG, the Volmer step was accelerated for which H* was easily to be generated for H₂ formation. This is the solid evidence to verify the synergistic effect between Ru SASs and NPs.

In addition, the excellent catalytic activity of Ru SASs +NPs/NG was further characterized in different aspects. We normalized the current density of the LSV curves obtained into the mass of metal to exclude the influence of metal loading and to elucidate the utilization of active sites. Clearly, the Ru SASs+NPs/NG (1.21 wt%) presented the highest mass activity with 12.57 A mg⁻¹_Ru at 100 mV, which was 23.3 and 12.7 times higher than that of Pt/C (0.54 A mg⁻¹_Pt) and Ru/C (0.99 A mg⁻¹_Ru), respectively (Figure 3d). The ECSA and TOF were adopted to further investigate the intrinsic catalytic activity. Here, the ECSA and the total catalytic site

number were evaluated by the underpotential deposition of Cu, with the detailed calculations shown in Figure S28 and Experimental section [34,49]. Clearly, the Ru SASs+NPs/ NG possessed a much larger ECSA (142.94 m^{-2} g^{-1}$_{metal}$) than the Ru SASs/NG (64.34 m^{-2} g^{-1}$_{metal}$), Pt/C (44.05 m^{-2} g^{-1}$_{metal}$) and Ru/C (17.6 m^{-2} g^{-1}$_{metal}$). Moreover, Brunauer-Emmett-Teller (BET) analysis *via* nitrogen adsorption-desorption isotherms revealed that the specific surface areas and pore structures of Ru SASs+NPs/NG and Ru SASs/NG are similar (Figure S29), suggesting that ECSA and HER activities are independent of the specific surface and pore size distribution. When the LSV curves were normalized to the ECSA (Figure S30), Ru SASs+NPs/NG still exhibited the highest catalytic current density, indicating the high atomic utilization and catalytic activity of the SASs+NPs structure. As shown in Figure 3e, the TOF values of Ru SASs+NPs/NG were 7 and 21 H$_2$ s^{-1} at 50 and 100 mV, respectively, which were 6 and 7.2 times those of Pt/C (1.1 and 2.9 H$_2$ s^{-1}) and also surpassed those of the state-of-the-art catalysts in literature (Table S3). This phenomenon suggests that combining Ru SASs and Ru NPs accelerated the reactive kinetics. In addition, electrochemical impedance spectroscopy (EIS) measurement at η=100 mV was further studied (Figure 3f). Meanwhile, the circuit model fitting was shown in Figure S31 and Table S4. The lowest charge transfer resistance (R_{CT}) of Ru SASs+NPs/NG indicated the fastest electron transfer rate, which again verified the faster reactive kinetics of Ru SASs+NPs/NG.

In terms of the long-term stability test, only a negligible decay was observed during the long-term electrolysis of Ru SASs+NPs/NG (Figure 3g) at 10 mA cm^{-2}, indicating the excellent stability of Ru SASs+NPs/NG. Beyond this, the Ru SASs+NPs/NG exhibited negligible performance degradation after 5,000 LSV sweeps, while there was some clear attenuation for Ru SASs/NG and Pt/C (insert in Figure 3g). Following the long-term durability test, the Ru SASs and Ru NPs in Ru SASs+NPs/NG maintained a good dispersion on the graphene matrix without aggregation (Figure S32), with the Ru SASs maintaining their primary form without aggregating into Ru clusters or NPs (Figure S33). However, severe agglomeration occurred in commercial Pt/C (Figure S34).

3.3   Theoretical study

DFT calculations were used to further illustrate the catalytic mechanism and activity origination of Ru SASs+NPs/NG. The calculation models are shown in Figure S35.

Here, the DFT structure optimization suggested that H$_2$O tended to be adsorbed on the Ru NPs rather than RuN$_4$ site, and H$^+$ tended to be adsorbed on RuN$_4$ site. Furthermore, H$_2$O was proven to tend to be adsorbed on Ru atom located at the interface of Ru NPs and graphene (Figure S36). Thus, Ru NPs promoted Volmer step to generate H* on the RuN$_4$ sites

(Figure 4a), which is likely to improve the HER activity in alkaline solutions. In the absence of Ru NPs, Volmer step is difficult to occur (Figure 4b). Subsequently, the free energy of hydrogen adsorption (ΔG_H*) was calculated according to the models shown in Figures S37 and S38. Here, the optimal ΔG_H* should be ~0 eV, whereas a conversely negative or positive ΔG_H* leads to too strong or too weak adsorption, respectively, of the intermediate H atoms [20,50,51]. As shown in Figure 4c and Table S5, the ΔG_H* of the RuN$_4$ in Ru SASs/NG was calculated to be −0.854 eV, indicating the strong adsorption of H* obstacles in H$_2$ formation and desorption. However, the ΔG_H* of the RuN$_4$ site in Ru SASs +NPs/NG was −0.423 eV, which is much closer to 0 eV, suggesting that the strong electronic interaction between RuN$_4$ and Ru NPs optimized the electronic structure of the RuN$_4$, thus suitably weakening the excessively strong adsorption of H on RuN$_4$ and ultimately promoting the HER activity in alkaline solutions. To ascertain the intrinsic reason behind this variation, the electronic structures of the RuN$_4$ site in Ru SASs+NPs/NG and Ru SASs/NG with H* were investigated using partial density of states (PDOS) analysis. As shown in Figure S39, the 4d electron configuration of the Ru in RuN$_4$ site was altered by the Ru NPs, indicating that the strong electronic interaction between RuN$_4$ site and Ru NPs rendered the charge to be re-distributed, which plays an important role in HER [52]. This issue was further clarified in Figure 4d and e. The overlapped degree of the Ru 4d (RuN$_4$ site) and H 1s in Ru SASs+NPs/NG was smaller than that in Ru SASs/NG, suggesting that the electronic interaction between Ru SASs and Ru NPs dampens the bonding of Ru 4d and the H 1s orbital, thus resolving the issue of excessive H adsorption strength on RuN$_4$ site and consequently promoting the HER process. Moreover, Pt still presents optimal ΔG_H* (−0.121 eV) than Ru according to the previous study [15], manifested as the fact that HER activity of Pt/C in 0.5 M H$_2$SO$_4$ was better than that of Ru SASs+NPs/NG (Figure S40) but the opposite in 1 M KOH solution demonstrating that water splitting is a much crucial factor for HER in alkaline.

Furthermore, the difference of HER activity between Ru SASs+NPs/NG and Pt/C was also studied. Since both Ru SASs+NPs/NG and Pt/C obey Volmer-Heyrovskey route with the Heyrovsky step denoted by the RDS, the activation energies of Heyrovskey step for Ru SASs+NPs/NG and Pt/C were also calculated and compared. As shown in Figure 4f (the calculation models are shown in Figures S41 and S42), the energy barrier of the Heyrovsky step in Ru SASs+NPs/ NG was calculated to be 0.42 eV (40.52 kJ mol^{-1}), which was much lower than that of Pt/C (1.30 eV, 125.9 kJ mol^{-1}), as calculated according to our previous study [17]. Because the activation energy of RDS is much lower, Ru SASs+NPs/ NG presents better HER activity than Pt/C, which is in accord with the experimental results.
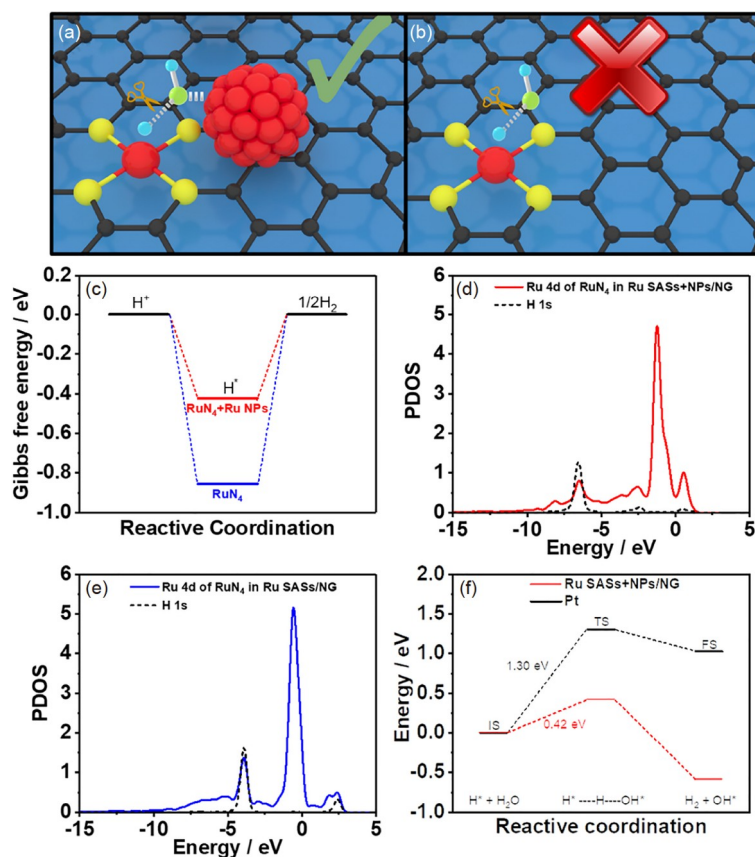
Figure 4 Water dissociation on (a) Ru SASs+NPs/NG and (b) Ru SASs/NG; (c) calculated free energy diagrams of hydrogen adsorption for RuN$_4$ and RuN$_4$+Ru NPs; Partial density of states (PDOS) of the Ru 4d of RuN$_4$ and H 1s in (d) Ru SASs+NPs/NG and (e) Ru SASs/NG with adsorbed hydrogen; (f) activation energy diagram of the Heyrovsky step on Ru SASs+NPs/NG and Pt/C (color online).

4　Conclusions

In summary, we successfully regulated the morphological distribution of Ru on graphene *via* ZIF-8-assisted pyrolysis. The cation exchange and host-guest strategies resulted in different interactions between ZIF-8 and Ru precursor, with two types of morphological distributions of Ru formed: Ru SASs combined with Ru NPs on the NG (Ru SASs+NPs/NG), and Ru SASs on the NG (Ru SASs/NG), in which Ru SASs+NPs/NG represents the best catalytic activity. This was due to two main factors: (1) the formation of Ru NPs appropriately reduces the energy barrier for water dissociation in alkaline solutions; (2) Ru NPs weaken the excessively strong adsorption of hydrogen on Ru SASs, resulting in outstanding HER performances of Ru SASs+NPs/NG in alkaline solutions. Overall, this study is expected to provide unique innovations for the development of catalysts for the HER in alkaline solutions.

1　Shi Y, Li M, Yu Y, Zhang B. *Energy Environ Sci*, 2020, 13: 4564–4582
2　Lagadec MF, Grimaud A. *Nat Mater*, 2020, 19: 1140–1150
3　de Luna P, Hahn C, Higgins D, Jaffer SA, Jaramillo TF, Sargent EH. *Science*, 2019, 364: eaav3506
4　Liu C, Gong T, Zhang J, Zheng X, Mao J, Liu H, Li Y, Hao Q. *Appl Catal B-Environ*, 2020, 262: 118245
5　Sarwar S, Nautiyal A, Cook J, Yuan Y, Li J, Uprety S, Shahbazian-Yassar R, Wang R, Park M, Bozack MJ, Zhang X. *Sci China Mater*, 2019, 63: 62–74
6　Cao Y, Liu H, Bo X, Wang F. *Sci China Chem*, 2015, 58: 501–507
7　Lee DK, Lee D, Lumley MA, Choi KS. *Chem Soc Rev*, 2019, 48: 2126–2157
8　Anantharaj S, Noda S, Jothi VR, Yi SC, Driess M, Menezes PW.

Angew Chem Int Ed, 2021, 60: 18981–19006

9   Zhao Z, Liu H, Gao W, Xue W, Liu Z, Huang J, Pan X, Huang Y. *J Am Chem Soc*, 2018, 140: 9046–9050

10 Zhao X, Zhang Z, Cao X, Hu J, Wu X, Ng AYR, Lu GP, Chen Z. *Appl Catal B-Environ*, 2020, 260: 118156

11 Feng Q, Wang Q, Zhang Z, Xiong Y, Li H, Yao Y, Yuan XZ, Williams MC, Gu M, Chen H, Li H, Wang H. *Appl Catal B-Environ*, 2019, 244: 494–501

12 Khan MA, Zhao H, Zou W, Chen Z, Cao W, Fang J, Xu J, Zhang L, Zhang J. *Electrochem Energ Rev*, 2018, 1: 483–530

13 Ali A, Shen PK. *Electrochem Energ Rev*, 2020, 3: 370–394

14 Ledezma-Yanez I, Wallace WDZ, Sebastián-Pascual P, Climent V, Feliu JM, Koper MTM. *Nat Energy*, 2017, 2: 17031

15 Durst J, Siebel A, Simon C, Hasché F, Herranz J, Gasteiger HA. *Energy Environ Sci*, 2014, 7: 2255–2260

16 Subbaraman R, Tripkovic D, Strmcnik D, Chang KC, Uchimura M, Paulikas AP, Stamenkovic V, Markovic NM. *Science*, 2011, 334: 1256–1260

17 Ye S, Luo F, Xu T, Zhang P, Shi H, Qin S, Wu J, He C, Ouyang X, Zhang Q, Liu J, Sun X. *Nano Energy*, 2020, 68: 104301

18 Zheng Y, Jiao Y, Vasileff A, Qiao SZ. *Angew Chem Int Ed*, 2018, 57: 7568–7579

19 Li L, Wang P, Shao Q, Huang X. *Chem Soc Rev*, 2020, 49: 3072–3106

20 Ye S, Luo F, Zhang Q, Zhang P, Xu T, Wang Q, He D, Guo L, Zhang Y, He C, Ouyang X, Gu M, Liu J, Sun X. *Energy Environ Sci*, 2019, 12: 1000–1007

21 Zhao D, Zhuang Z, Cao X, Zhang C, Peng Q, Chen C, Li Y. *Chem Soc Rev*, 2020, 49: 2215–2264

22 Song Z, Zhang L, Doyle-Davis K, Fu X, Luo JL, Sun X. *Adv Energy Mater*, 2020, 10: 2215–2264

23 Zhuo HY, Zhang X, Liang JX, Yu Q, Xiao H, Li J. *Chem Rev*, 2020, 120: 12315–12341

24 Qin T, Wang Z, Wang Y, Besenbacher F, Otyepka M, Dong M. *Nano-Micro Lett*, 2021, 13: 183

25 Zhang L, Jia Y, Gao G, Yan X, Chen N, Chen J, Soo MT, Wood B, Yang D, Du A, Yao X. *Chem*, 2018, 4: 285–297

26 Zeng X, Shui J, Liu X, Liu Q, Li Y, Shang J, Zheng L, Yu R. *Adv Energy Mater*, 2018, 8: 1701345

27 Yang J, Chen B, Liu X, Liu W, Li Z, Dong J, Chen W, Yan W, Yao T, Duan X, Wu Y, Li Y. *Angew Chem Int Ed*, 2018, 57: 9495–9500

28 Hui L, Xue Y, Yu H, Liu Y, Fang Y, Xing C, Huang B, Li Y. *J Am Chem Soc*, 2019, 141: 10677–10683

29 Chen W, Pei J, He CT, Wan J, Ren H, Wang Y, Dong J, Wu K, Cheong WC, Mao J, Zheng X, Yan W, Zhuang Z, Chen C, Peng Q, Wang D, Li Y. *Adv Mater*, 2018, 30: 1800396

30 Sun T, Zhao S, Chen W, Zhai D, Dong J, Wang Y, Zhang S, Han A, Gu L, Yu R, Wen X, Ren H, Xu L, Chen C, Peng Q, Wang D, Li Y. *Proc Natl Acad Sci USA*, 2018, 115: 12692–12697

31 Wen Y, Qi J, Zhao D, Liu J, Wei P, Kang X, Li X. *Appl Catal B-Environ*, 2021, 293: 120196

32 Fang Y, Sun D, Niu S, Cai J, Zang Y, Wu Y, Zhu L, Xie Y, Liu Y, Zhu Z, Mosallanezhad A, Niu D, Lu Z, Shi J, Liu X, Rao D, Wang G, Qian Y. *Sci China Chem*, 2020, 63: 1563–1569

33 Xiong F, Wang Z, Wu Z, Sun G, Xu H, Chai P, Huang W. *Sci China Chem*, 2019, 62: 199–204

34 Zheng Y, Jiao Y, Zhu Y, Li LH, Han Y, Chen Y, Jaroniec M, Qiao SZ. *J Am Chem Soc*, 2016, 138: 16174–16181

35 Green CL, Kucernak A. *J Phys Chem B*, 2002, 106: 1036–1047

36 Segall MD, Lindan PJD, Probert MJ, Pickard CJ, Hasnip PJ, Clark SJ, Payne MC. *J Phys-Condens Matter*, 2002, 14: 2717–2744

37 Hamann DR, Schlüter M, Chiang C. *Phys Rev Lett*, 1979, 43: 1494–1497

38 Voiry D, Yamaguchi H, Li J, Silva R, Alves DCB, Fujita T, Chen M, Asefa T, Shenoy VB, Eda G, Chhowalla M. *Nat Mater*, 2013, 12: 850–855

39 Kresse G, Furthmüller J. *Phys Rev B*, 1996, 54: 11169–11186

40 Kresse G, Furthmüller J. *Comput Mater Sci*, 1996, 6: 15–50

41 Perdew JP, Burke K, Ernzerhof M. *Phys Rev Lett*, 1996, 77: 3865–3868

42 Perdew JP, Ernzerhof M, Burke K. *J Chem Phys*, 1996, 105: 9982–9985

43 Grimme S. *J Comput Chem*, 2006, 27: 1787–1799

44 Xiao M, Gao L, Wang Y, Wang X, Zhu J, Jin Z, Liu C, Chen H, Li G, Ge J, He Q, Wu Z, Chen Z, Xing W. *J Am Chem Soc*, 2019, 141: 19800–19806

45 Zhang Y, Wang P, Yang J, Lu S, Li K, Liu G, Duan Y, Qiu J. *Curr Alzheimer Resbon*, 2021, 177: 344–356

46 Ding B, Fan Z, Lin Q, Wang J, Chang Z, Li T, Henzie J, Kim J, Dou H, Zhang X, Yamauchi Y. *Small Methods*, 2019, 3: 1900277

47 Kunitski M, Eicke N, Huber P, Köhler J, Zeller S, Voigtsberger J, Schlott N, Henrichs K, Sann H, Trinter F, Schmidt LPH, Kalinin A, Schöffler MS, Jahnke T, Lein M, Dörner R. *Nat Commun*, 2019, 10: 1

48 Hu Q, Li G, Huang X, Wang Z, Yang H, Zhang Q, Liu J, He C. *J Mater Chem A*, 2019, 7: 19531–19538

49 Li J, Zhang H, Samarakoon W, Shan W, Cullen DA, Karakalos S, Chen M, Gu D, More KL, Wang G, Feng Z, Wang Z, Wu G. *Angew Chem Int Ed*, 2019, 58: 18971–18980

50 Jiao Y, Zheng Y, Davey K, Qiao SZ. *Nat Energy*, 2016, 1: 16130

51 Jiao Y, Zheng Y, Jaroniec M, Qiao SZ. *Chem Soc Rev*, 2015, 44: 2060–2086

52 Wang Z, Wu H, Li Q, Besenbacher F, Li Y, Zeng X, Dong M. *Adv Sci*, 2020, 7: 1901382